# Modeling Gas-Particle Two-Phase Flows with Complex and Moving Boundaries using DEM-CFD with an Immersed Boundary Method

**Y. Guo, C. -Y. Wu, and C. Thornton**
School of Chemical Engineering, University of Birmingham, Birmingham, B15 2TT, U.K.

*DOI 10.1002/aic.13900*
*Published online August 20, 2012 in Wiley Online Library (wileyonlinelibrary.com).*

*An immersed boundary method (IBM) has been developed and incorporated into the coupled discrete element method and computational fluid dynamics (DEM-CFD) approach to model particulate systems consisting of a compressible gas and solid particles with complex and/or moving boundaries. The IBM is used to deal with the interaction between gas and complex and moving boundaries by using simple rectangular grids to discretize the fluid field. The developed method has been applied to simulate some typical powder handling processes (e.g., gas fluidization with an immersed tube, segregation in a vertically vibrated bed, and pneumatic conveying). Good agreement is achieved between the present simulation results and the experimental ones reported in the literature. It has been demonstrated that the capacity of DEM-CFD is enhanced with the incorporation of IBM, which can be used to simulate a wide range of problems that could not be handled with the conventional DEM-CFD method.* © 2012 American Institute of Chemical Engineers *AIChE J,* 59: 1075–1087, 2013
*Keywords: two-phase flow, complex/moving boundaries, immersed boundary method, discrete element method, computational fluid dynamics*

## Introduction

Fluid-solid particle two-phase flows are ubiquitous in industrial applications and biological systems, such as gas fluidization, pneumatic conveying, die filling, and blood flow. Understanding the two-phase flow behavior in these processes is crucial for the design of industrial equipment and revealing the operative mechanisms of biological systems. In recent years, a coupled discrete element method (DEM) and computational fluid dynamics (CFD) approach has been widely used to model fluid-solid particle flow problems,[1] since it was first introduced by Tsuji et al.[2,3] In this method, two-way coupling of fluid–particle interaction is considered, and both fluid and particle can be analyzed in detail.

In general, fixed and rectangular grids were used in the coupled DEM-CFD method for the discretization of fluid domain due to the simple numerical implementation and low computational cost. However, difficulties arise when dealing with complex and/or moving boundaries that do not conform to the grids. However, this problem can be resolved with using an immersed boundary method (IBM) that was first proposed by Peskin[4] and allows the use of rectangular grids for arbitrarily complex geometries. IBM has since been applied to model incompressible flows primarily[4–11] and was advanced to compressible flows recently.[12–14]

The main idea of this method is to introduce a virtual body force field such that a desired fluid velocity distribution can be imposed over a solid boundary. The virtual body force field is normally determined by two major methods: feedback forcing and direct forcing.[7] The feedback forcing method has been successfully applied to simulate biological and multiphase flows with elastic boundaries.[4,5] In this method, two adjustable parameters need to be tuned for the feedback force according to the frequency of flow. For a strongly unsteady flow, the adjustable parameters have to be sufficiently large to restore force at a frequency which is higher than any frequency in the flow.[7] This leads to much stiffer governing equations for the fluid so that very small time steps are required for the time integration. Mohd-Yusof [6] has derived an alternative formulation of the forcing, that is, direct forcing, which does not involve any adjustable parameters and has no influence on the stability of the time integration scheme. In the direct forcing method, the forcing is introduced at the first grid points external to the solid body by assigning them velocities obtained by the interpolation of the velocities at the second grid points and at the solid boundary. Recently, Kajishima et al.[10] and Yuki et al.[11] proposed that the forcing applied to a fluid cell can be simply approximated by the solid volumetric fraction and the relative velocity of two phases in that cell. By comparison, the IBM with this forcing method produced nearly the same results as the IBM with the direct forcing method in modeling fluid flow past a circular cylinder,[11] but the former is much more computationally efficient than the latter.

In this study, the IBM introduced by Kajishima et al.[10] and Yuki et al.[11] for incompressible flows has been extended and incorporated into our existing DEM-CFD code[15] to simulate slightly compressible gas-particle two-phase flows with

Correspondence concerning this article should be addressed to C.-Y. Wu at C.Y.Wu@bham.ac.uk or Y. Guo at this current address: Chemical Engineering Dept., University of Florida, Gainesville, FL 32611; e-mail: guoyu03@gmail.com.

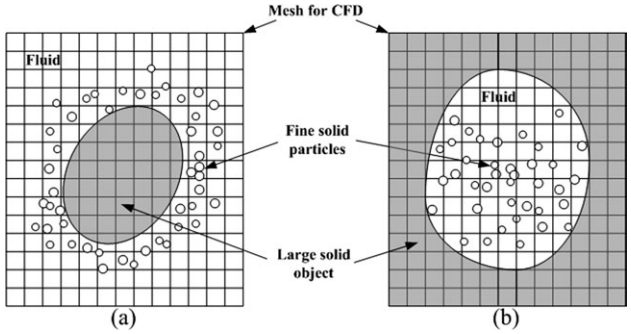


**Figure 1. Illustration of fluid-solid system with the fluid and fine solid particles outside (a) and inside (b) the LSO.**

complex and/or moving boundaries. This article is organized as follows: a comprehensive description of the governing equations and numerical approaches is presented first and, thereafter, several typical applications of the developed method such as gas fluidization with an immersed tube, segregation in a vertically vibrated bed, and pneumatic conveying in a cylindrical pipeline are illustrated and discussed. Finally, conclusions are drawn.

## Governing Equations and Numerical Method

The typical multiphase system considered involves a fluid, many fine solid particles, and one or more large solid objects (LSOs), as shown in Figure 1. The fluid and fine solid particles can be present outside or inside the LSOs. The fluid dynamics is analyzed using CFD, and the motions of individual solids are analyzed using DEM. The interactions between the fluid and the fine particles (the number of which could be large) are approximated by an empirical drag force model for reducing computational cost, although the detailed information on how the fluid flows around a single particle cannot be resolved using this method. However, when a LSO is present in the system, the detailed information of fluid flow near the LSO could become crucial when determining the macroscopic behavior of the multiphase system. Under this condition, the surface of the LSO should be treated as the solid boundary for the fluid flow. Therefore, an IBM is developed to model the interaction between the fluid and LSOs, with which the fluid flow can be resolved to the boundary layer scale. A further cost benefit of IBM is the ability to deal with complex and/or moving boundaries using simple rectangular grids.

### *Motion of fine solid particles*

The translational and rotational motions of each fine spherical particle are governed by Newton's equations of motion

$$m_{\mathrm{i}}\frac{d\boldsymbol{v}_{\mathrm{i}}}{dt}=\mathbf{f}_{\mathrm{ci}}+\mathbf{f}_{\mathrm{fpi}}+m_{\mathrm{i}}\mathbf{g} \tag{1}$$

$$I_{\mathrm{i}}\frac{d\boldsymbol{\omega}_{\mathrm{i}}}{dt}=\mathbf{T}_{\mathrm{i}} \tag{2}$$

in which $m_{\mathrm{i}}$, $I_{\mathrm{i}}$, $\boldsymbol{v}_{\mathrm{i}}$ and $\boldsymbol{\omega}_{\mathrm{i}}$ are the mass, moment of inertia, linear velocity, and angular velocity, respectively, of the particle $i$, g is the gravitational acceleration, $\mathbf{f}_{\mathrm{ci}}$ is the sum of the interparticle contact forces and the particle-LSO contact force, and $\mathbf{f}_{\mathrm{fpi}}$ is the fluid-particle interaction force, and $\mathbf{T}_{\mathrm{i}}$ represents the torque arising from the tangential components of the contact forces. The particles considered in this study are assumed to be elastic and frictional, and the calculations of the interparticle and the particle-LSO contact forces are based on classical contact mechanics theory,[16] in which the theory of Hertz[17] is used to determine the normal force and the theory of Mindlin and Deresiewicz[18] is used for modeling the tangential force.

### *Fluid–fine solid particle interaction*

The fluid field is resolved at the scale of the computational fluid cells, whose sizes are larger than the fine solid particles (Figure 1). Therefore, it is impossible to extract the detailed fluid flow around a single particle. However, the resultant force of the interaction between the fluid and each fine solid particle can be evaluated based on the size and velocity of the particle and the local fluid variables averaged over the fluid cell in which the particle resides. According to Anderson and Jackson,[19] this force may be expressed as

$$\mathbf{f}_{\mathrm{fpi}}=-v_{\mathrm{pi}}\nabla p+v_{\mathrm{pi}}\nabla\cdot\boldsymbol{\tau}_{\mathrm{f}}+\varepsilon\mathbf{f}_{\mathrm{di}} \tag{3}$$

where $v_{\mathrm{pi}}$ is the volume of particle $i$, $p$, and $\boldsymbol{\tau}_{\mathrm{f}}$ are the local fluid pressure and viscous stress tensor, $\varepsilon$ is the local void fraction, and $\mathbf{f}_{\mathrm{di}}$ represents the drag force acting on particle $i$.

Assuming a Newtonian flow, the viscous stress tensor $\boldsymbol{\tau}_{\mathrm{f}}$, can be written as

$$\boldsymbol{\tau}_{\mathrm{f}}=\left[\left(\mu_{\mathrm{b}}-\frac{2}{3}\mu_{\mathrm{s}}\right)\nabla\cdot\mathbf{u}_{\mathrm{f}}\right]\boldsymbol{\delta}+\mu_{\mathrm{s}}\left[(\nabla\mathbf{u}_{\mathrm{f}})+(\nabla\mathbf{u}_{\mathrm{f}})^{\mathrm{T}}\right] \tag{4}$$

where $\mathbf{u}_{\mathrm{f}}$ is the fluid velocity, $\mu_{\mathrm{b}}$ and $\mu_{\mathrm{s}}$ are the bulk viscosity and shear viscosity, respectively, and $\boldsymbol{\delta}$ is the identity tensor.

For the flow of a fluid through a packed bed of fine particles, Di Felice[20] proposed an empirical correlation to calculate the drag force, $\mathbf{f}_{\mathrm{di}}$, acting on an individual particle as follows

$$\mathbf{f}_{\mathrm{di}}=\frac{1}{2}C_{\mathrm{Di}}\rho_{\mathrm{fj}}\frac{\pi d_{\mathrm{pi}}^2}{4}\varepsilon_{\mathrm{j}}^2|\mathbf{u}_{\mathrm{fj}}-\mathbf{v}_{\mathrm{i}}|(\mathbf{u}_{\mathrm{fj}}-\mathbf{v}_{\mathrm{i}})\varepsilon_{\mathrm{j}}^{-(\vartheta+1)} \tag{5}$$

where, $\rho_{\mathrm{fj}}$, $\mathbf{u}_{\mathrm{fj}}$ and $\varepsilon_{\mathrm{j}}$ are the fluid density, fluid velocity, and void fraction of the fluid cell $j$ in which particle $i$ of diameter $d_{\mathrm{pi}}$ resides, and $C_{\mathrm{Di}}$ is the fluid drag coefficient for a single unhindered particle. The void fraction function $\varepsilon_{\mathrm{j}}^{-(\vartheta+1)}$ corrects for the presence of other particles. The parameters $C_{\mathrm{Di}}$ and $\vartheta$ can be expressed as the functions of the Reynolds number of particle $i$ (see Di Felice[20]).

### *Fluid flow*

The dynamics of a compressible fluid in a particulate system is governed by the following continuity and momentum equations

$$\frac{\partial(\varepsilon\rho_{\mathrm{f}})}{\partial t}+\nabla\cdot(\varepsilon\rho_{\mathrm{f}}\mathbf{u}_{\mathrm{f}})=0 \tag{6}$$

$$\frac{\partial(\varepsilon\rho_{\mathrm{f}}\mathbf{u}_{\mathrm{f}})}{\partial t}+\nabla\cdot(\varepsilon\rho_{\mathrm{f}}\mathbf{u}_{\mathrm{f}}\mathbf{u}_{\mathrm{f}})=-\nabla p+\nabla\cdot\boldsymbol{\tau}_{\mathrm{f}}-\mathbf{F}_{\mathrm{fp}}+\varepsilon\rho_{\mathrm{f}}\mathbf{g} \tag{7}$$

in which, the fluid–particle interaction force per unit volume $\mathbf{F}_{\mathrm{fp}}$, is obtained by summing up all the $\mathbf{f}_{\mathrm{fpi}}$ in a fluid cell,

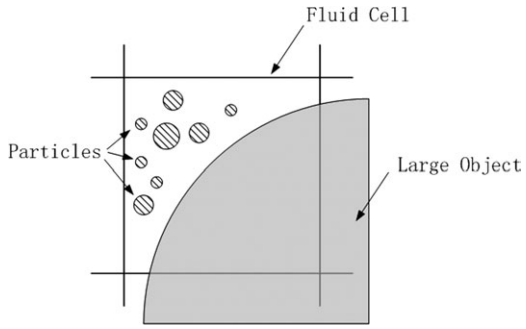


**Figure 2. Illustration of the immersion of the fine particles and large object in a fluid cell.**

defined by Eq. 3, and dividing by the volume of the fluid cell, $V_{\text{cell}}$, thus

$$\mathbf{F}_{\text{fp}} = \frac{1}{V_{\text{cell}}} \sum\nolimits_{\text{i}=1}^{n_{\text{c}}} \mathbf{f}_{\text{fpi}} \tag{8}$$

where, $n_{\text{c}}$ is the number of particle contacts in that fluid cell.

By substituting Eq. 3, Eq. 8 has the form

$$\mathbf{F}_{\text{fp}} = -(1-\varepsilon)\nabla p + (1-\varepsilon)\nabla \cdot \tau_{\text{f}} + \frac{1}{V_{\text{cell}}} \sum\nolimits_{\text{i}=1}^{n_{\text{c}}} \varepsilon \mathbf{f}_{\text{di}} \tag{9}$$

Substituting Eq. 9 into Eq. 7, the momentum equation can be expressed as

$$\frac{\partial(\varepsilon\rho_{\text{f}}\mathbf{u}_{\text{f}})}{\partial t} + \nabla \cdot (\varepsilon\rho_{\text{f}}\mathbf{u}_{\text{f}}\mathbf{u}_{\text{f}}) = -\varepsilon\nabla p + \varepsilon\nabla \cdot \tau_{\text{f}} - \mathbf{F}^{*}_{\text{fp}} + \varepsilon\rho_{\text{f}}\mathbf{g} \tag{10}$$

in which

$$\mathbf{F}^{*}_{\text{fp}} = \frac{1}{V_{\text{cell}}} \sum\nolimits_{\text{i}=1}^{n_{\text{c}}} \varepsilon \mathbf{f}_{\text{di}} \tag{11}$$

In this work, gas-solid particle two-phase flows are studied and the ideal gas law is adopted to evaluate the gas density, which could change due to the compressibility

$$\rho_{\text{f}} = \frac{M_{\text{f}}}{RT} p \tag{12}$$

where $M_{\text{f}}$ is the average molar mass of gas (0.0288 kg mol$^{-1}$ for air), $R$ is the ideal gas constant (8.314472 J K$^{-1}$ mol$^{-1}$), and $T$ is the gas temperature.

### *Immersed boundary method*

An IBM, which was proposed by Kajishima et al.[10] for incompressible flows, is developed for modeling particulate systems consisting of gas and solid particles. Before deriving the governing equations, some useful parameters need to be defined first. As illustrated in Figure 2, the volume of a single fluid cell, $V_{\text{cell}}$, can be expressed as the sum of the volume of the fine particles, $V_{\text{p}}$, the volume of the LSO, $V_{\text{obj}}$, and the volume of the fluid in this cell, $V_{\text{f}}$. Therefore,

$$V_{\text{cell}} = V_{\text{p}} + V_{\text{obj}} + V_{\text{f}} \tag{13}$$

The volume fraction of the space excluding the fine particles in a fluid cell is defined as the effective void fraction, which can be written as

$$\varepsilon_{\text{e}} = 1 - \frac{V_{\text{p}}}{V_{\text{cell}}} = \frac{V_{\text{obj}} + V_{\text{f}}}{V_{\text{cell}}} \tag{14}$$

In addition, the volume fraction of the LSO in a cell can be written as

$$\alpha = \frac{V_{\text{obj}}}{V_{\text{cell}}} \tag{15}$$

Based on the work of Kajishima et al.,[10] a unified velocity field, $\mathbf{u}$, is established to describe the fluid-LSO system by volume averaging the local fluid velocity, $\mathbf{u}_{\text{f}}$, and the local solid object velocity, $\mathbf{U}_{\text{obj}}$, for each fluid cell, that is,

$$\mathbf{u} = \frac{V_{\text{f}}}{V_{\text{obj}} + V_{\text{f}}}\mathbf{u}_{\text{f}} + \frac{V_{\text{obj}}}{V_{\text{obj}} + V_{\text{f}}}\mathbf{U}_{\text{obj}} = \frac{\varepsilon_{\text{e}} - \alpha}{\varepsilon_{\text{e}}}\mathbf{u}_{\text{f}} + \frac{\alpha}{\varepsilon_{\text{e}}}\mathbf{U}_{\text{obj}} \tag{16}$$

The local solid object velocity, $\mathbf{U}_{\text{obj}}$, can be obtained by averaging the local velocities of solid points over the volume of the LSO falling in a local fluid cell, $V_{\text{obj}}$, that is,

$$\mathbf{U}_{\text{obj}} = \frac{1}{V_{\text{obj}}} \int_{V_{\text{obj}}} (\mathbf{v}_{\text{LOS}} + \boldsymbol{\omega}_{\text{LSO}} \times \mathbf{r}) dV = \mathbf{v}_{\text{LSO}} + \frac{1}{V_{\text{obj}}} \int_{V_{\text{obj}}} \boldsymbol{\omega}_{\text{LSO}} \times \mathbf{r} dV \tag{17}$$

in which, $\boldsymbol{v}_{\text{LSO}}$ and $\boldsymbol{\omega}_{\text{LSO}}$ are the translational and rotational velocities of the LSO and $\mathbf{r}$ is the relative position from the centre of mass of the object to a local point on the object.

By assuming the no-slip and impermeable conditions at the fluid-solid interface ($\mathbf{u}_{\text{f}} = \mathbf{U}_{\text{obj}}$), the fluid-LSO as a whole can be treated as a single continuum with a unified velocity field, $\mathbf{u}$, which satisfies the following continuity and momentum equations

$$\frac{\partial(\varepsilon_{\text{e}}\rho_{\text{f}})}{\partial t} + \nabla \cdot (\varepsilon_{\text{e}}\rho_{\text{f}}\mathbf{u}) = 0 \tag{18}$$

$$\frac{\partial(\varepsilon_{\text{e}}\rho_{\text{f}}\mathbf{u})}{\partial t} + \nabla \cdot (\varepsilon_{\text{e}}\rho_{\text{f}}\mathbf{u}\mathbf{u}) = -\varepsilon_{\text{e}}\nabla p + \varepsilon_{\text{e}}\nabla \cdot \boldsymbol{\tau} - \mathbf{F}^{*}_{\text{fp}} + \varepsilon_{\text{e}}\rho_{\text{f}}\mathbf{g} + \mathbf{f}' \tag{19}$$

in which $\boldsymbol{\tau}$ is given by Eq. 4 but with $\mathbf{u}$ replacing $\mathbf{u}_{\text{f}}$. The effective void fraction, $\varepsilon_{\text{e}}$, is used in the above two governing equations to account for the effect of the presence of fine particles. However, in using Eq. 11 to calculate $\mathbf{F}^{*}_{\text{fp}}$ and Eq. 5 to calculate the drag force $\mathbf{f}_{\text{di}}$, the real void fraction is used and obtained from

$$\varepsilon = 1 - \frac{V_{\text{p}}}{V_{\text{cell}} - V_{\text{obj}}} = \frac{\varepsilon_{\text{e}} - \alpha}{1 - \alpha} \tag{20}$$

The momentum Eq. 19 is similar to Eq. 10 except for the virtual body force term, $\mathbf{f}'$, which is used to correct the velocity field, $\mathbf{u}$, at the fluid-solid interface and inside the LSO. Using a first-order finite difference algorithm, the momentum Eq. 19 can be discretized in time as follows

$$(\varepsilon_{\text{e}}\rho_{\text{f}}\mathbf{u})^{n+1} = (\varepsilon_{\text{e}}\rho_{\text{f}}\mathbf{u})^{n} + \Delta t \cdot \mathbf{H}^{n} - \Delta t \cdot (\varepsilon_{\text{e}}\nabla p)^{n+1} + \Delta t \cdot (\mathbf{f}')^{n+1} \tag{21}$$

where

$$\mathbf{H} = -\nabla \cdot (\varepsilon_{\text{e}}\rho_{\text{f}}\mathbf{u}\mathbf{u}) + \varepsilon_{\text{e}}\nabla \cdot \boldsymbol{\tau} - \mathbf{F}^{*}_{\text{fp}} + \varepsilon_{\text{e}}\rho_{\text{f}}\mathbf{g} \tag{22}$$

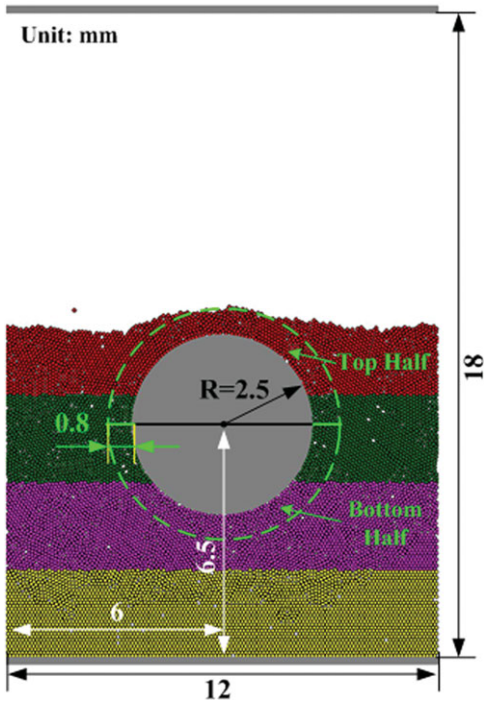


**Figure 3. Numerical model of the gas-fluidized bed with a static immersed tube.**

**The bed of 10,000 monosized particles ($d_p$ = 100 $\mu$m) was initially color-banded for visualizing the mixing patterns. Periodic boundary conditions were assigned to the lefthand and righthand side boundaries. Uniform gas was introduced at the bottom of the bed at a constant mass flow rate and exited from the top boundary across which zero gradients of velocity and pressure were assigned. The initial superficial gas velocity was 50 mm/s. [Color figure can be viewed in the online issue, which is available at wileyonlinelibrary.com.]**

and $\Delta t$ is the time step and superscripts indicate the number of the time step.

For the computational cells outside the LSO ($\alpha = 0$ and $\mathbf{u} = \mathbf{u}_f$), no virtual body forces exist, that is, $(\mathbf{f}')^{n+1} = 0$, and thereby the momentum Eq. 19 reduces to Eq. 10. For the cells inside the solid object ($\alpha = 1$), $\mathbf{u}$ is equal to $\mathbf{U}_{obj}$. Substituting $\mathbf{u}^{n+1} = \mathbf{U}_{obj}^{n+1}$, the virtual body forces, $\mathbf{f}'$, can be derived from Eq. 21 in the form of

$$(\mathbf{f}')^{n+1} = \frac{(\varepsilon_e \rho_f \mathbf{U}_{obj})^{n+1} - (\varepsilon_e \rho_f \mathbf{u})^n}{\Delta t} - \mathbf{H}^n + (\varepsilon_e \nabla p)^{n+1} \quad (23)$$

For the cells at the fluid-solid interface that are partially occupied by the LSO, that is, $0<\alpha<1$, the virtual body forces can be evaluated by a first-order linear interpolation using $\alpha$

$$(\mathbf{f}')^{n+1} = \alpha \left[ \frac{(\varepsilon_e \rho_f \mathbf{U}_{obj})^{n+1} - (\varepsilon_e \rho_f \mathbf{u})^n}{\Delta t} - \mathbf{H}^n + (\varepsilon_e \nabla p)^{n+1} \right] \quad (24)$$

**Table 1. Material Properties of the Particles and Tube for the Fluidization Simulations**

| | Density (Kg/m$^3$) | Young's modulus (GPa) | Poisson's ratio | Friction coefficient |
|---|---|---|---|---|
| Particles | 2500 | 8.7 | 0.3 | 0.3 (particle-particle) |
| Tube | 7900 | 210 | 0.29 | 0.3 (particle-tube) |

To evaluate $\alpha$ for the computational cells at the fluid-solid interface, Yuki et al.[11] proposed a simple algorithm as follows

$$\alpha = 0.5 \times \left[ 1 - \tanh\left( \frac{\Delta}{\sigma \lambda d_{cell}} \right) \right] \quad (25)$$

$$\lambda = |n_x| + |n_y| + |n_z| \quad (26)$$

$$\sigma = 0.05 \times (1 - \lambda^2) + 0.3 \quad (27)$$

in which $d_{cell}$ is the cell size, $\mathbf{n} = (n_x, n_y, n_z)$ is a normal outward unit vector at the surface element intersected by the cell, and $\Delta$ is a signed distance from the cell center to the surface element. This algorithm was reported to be applicable to the calculation of $\alpha$ for flow analyses involving arbitrary shaped and/or deformable solid objects and also it was proved computationally efficient due to the simplified formulation.[11]

### *Motion of LSO*

If the LSO neither remains static nor moves with a prescribed motion, its translational and rotational motions are governed by Newton's equations of motion

$$\frac{d(m_{LSO}\mathbf{v}_{LSO})}{dt} = -\int_{V_T} \mathbf{f}' dV + \mathbf{f}_c + m_{LSO}\mathbf{g} \quad (28)$$

$$\frac{d(\mathbf{I}_{LSO} \cdot \boldsymbol{\omega}_{LSO})}{dt} = -\int_{V_T} \mathbf{r} \times \mathbf{f}' dV + \mathbf{T}_c \quad (29)$$

in which, $m_{LSO}$ is the mass of the LSO. The first term on the righthand side of Eq. 28 is the integral of the virtual body force defined by Eqs. 23 and 24 over the total volume of the LSO, $V_T$. The parameter $\mathbf{f}_c$ represents the sum of contact forces exerted on the solid object from the fine particles. In Eq. 29, $\mathbf{I}_{LSO}$ is the moment of inertia tensor of the LSO. The first term on the righthand side of Eq. 29 is the integral of the moment due to the virtual body force over the total volume of the LSO, and $\mathbf{T}_c$ is the torque arising from the interactions between the fine particles and the LSO. By using the same virtual body force for the fluid and solid object in a shared cell, the conservation of momentum can be ensured during the momentum exchange between phases.[11]

### *Numerical procedure*

The motions of fine particles and LSO are solved by using a second-order central finite difference scheme to discretize the Newton's equations of motion. For the gas phase, the governing equations are solved using an adapted version of Patankar's SIMPLE algorithm, in which the gas is assumed to be slightly compressible, and besides the continuity equation and momentum equation, the ideal gas law Eq. 12 is also used to correlate the gas density and pressure. This adapted SIMPLE algorithm has been applied to model the gas-particle flows in fluidized beds[15] and die filling.[21,22] The numerical procedure for each time step of the proposed method is summarized as follows

**Table 2. Initial Conditions of the Gas**

| | Pressure (KPa) | Density (Kg/m$^3$) | Shear viscosity (Kg/ms) | Bulk viscosity (Kg/ms) | Temperature (K) |
|---|---|---|---|---|---|
| Gas | 101.325 | 1.2 | $1.8\times10^{-5}$ | 0 | 293 |

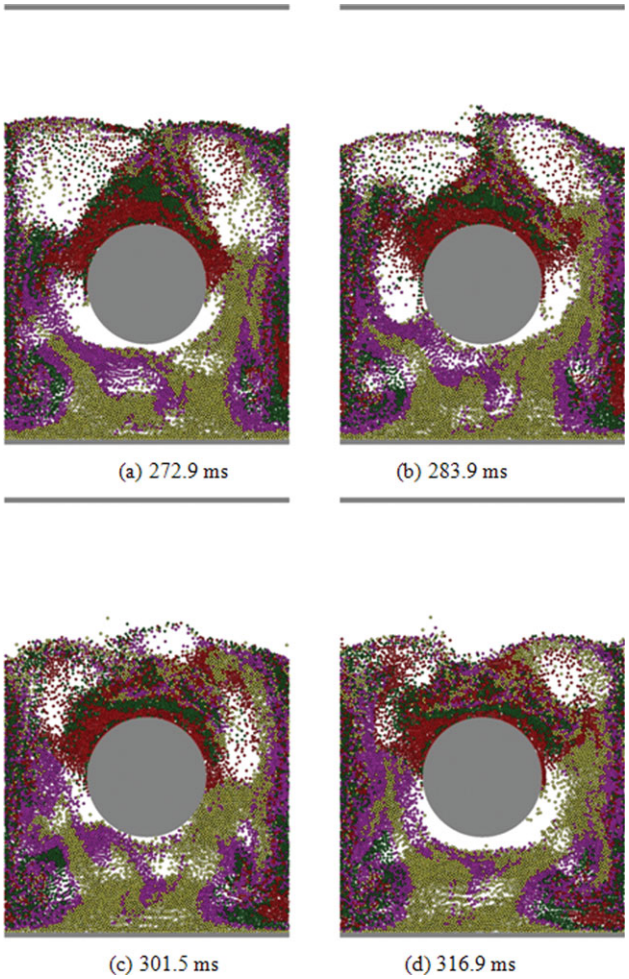


**Figure 4. Gas-fluidized bed with a static immersed tube.**

**The labels represent the elapsed time in millisecond (ms) after the start of fluidization. [Color figure can be viewed in the online issue, which is available at wileyonlinelibrary.com.]**

1. Calculate the new velocities and new positions of fine particles based on Eqs. 1 and 2.

2. Calculate the new velocity and new position of the LSO: (a) if the LSO keeps static, this step is skipped; (b) if its motion is prescribed, the calculation is based on the prescribed law of motion; and (c) if it moves freely, the calculation is according to Eqs. 28 and 29.

3. Calculate the current $\varepsilon_e$, $\alpha$, and $\varepsilon$ of each fluid cell.

4. Calculate the virtual body force, $(\mathbf{f}')^{n+1}$, from Eqs. 23 and 24 and the velocity field, $\mathbf{u}^{n+1}$, from 21 using current pressure field, $p^*$.

5. Establish the pressure-correction equations based on the continuity Eq. 18. The corrected pressure, $p'$, for each fluid cell can be solved from this set of linear equations. The derivation of the pressure-correction equations is provided in the Appendix.

6. Calculate the actual pressure field using $p^{n+1} = p^* + p'$.

7. Update $(\mathbf{f}')^{n+1}$ and $\mathbf{u}^{n+1}$ by substituting the actual pressure $p^{n+1}$ into Eqs. 23, 24, and 21.

8. Verify the convergence using the continuity Eq. 18. If the solution has not converged, the procedure is repeated from Step 4 by treating the newly obtained pressure, $p^{n+1}$, as the current pressure, $p^*$. This loop continues until the solution converges.

9. Extract the new fluid velocity, $\mathbf{u}_f^{n+1}$, from Eq. 16.

## Results and Discussion

Three case studies involving curved and/or moving boundaries were performed using the developed method. The first case is gas fluidization with an immersed tube, the second is the particle segregation in a vibrating bed, and the third is pneumatic conveying in a cylindrical pipe.

### *Fluidization with an immersed tube*

In some industrial fluidized bed reactors, tubes are immersed to provide or remove the heat. A number of experiments[23,24] have been conducted to explore the effects of immersed tubes on the fluidized behavior. In addition, some numerical investigations[25–27] have also been undertaken, from which some microscopic and dynamic information were obtained. Two major types of methods were used in the numerical studies: two-fluid modeling[27] and coupled DEM-CFD.[25,26] As argued by Yu and Xu,[28] the effective application of two-fluid modeling depends heavily on the constitutive relations for the solid particle phase and the momentum exchange between two phases, which are impossible to obtain within its framework. This becomes particularly true when dealing with different types of particles that should be treated as different phases. This drawback can be overcome by using the coupled DEM-CFD method. However, in previous DEM-CFD simulations of fluidized beds with immersed tubes, the surfaces of the cylindrical tubes did not conform to the rectangular grids. Consequently, nonsmooth stepwise boundaries were adopted for the fluid flow around the tubes.[25,26] This simplified treatment could result in significant errors in the numerical modeling. Fortunately, as discussed above, the effect of the immersion of solid boundaries within the fluid domain can be more accurately analyzed using the IBM. Furthermore, using IBM, moving

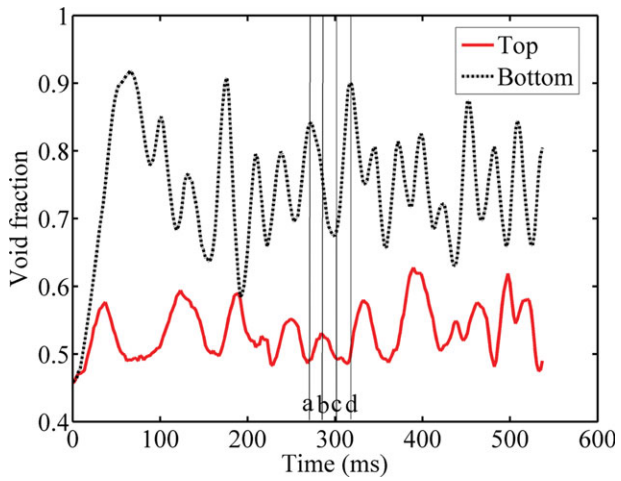


**Figure 5. Time evolution of void fraction in the top and bottom halves, respectively, of the annulus with a thickness of 0.8 mm (i.e., eight times the particle diameter) surrounding the tube (see Figure 3).**

**[Color figure can be viewed in the online issue, which is available at wileyonlinelibrary.com.]**

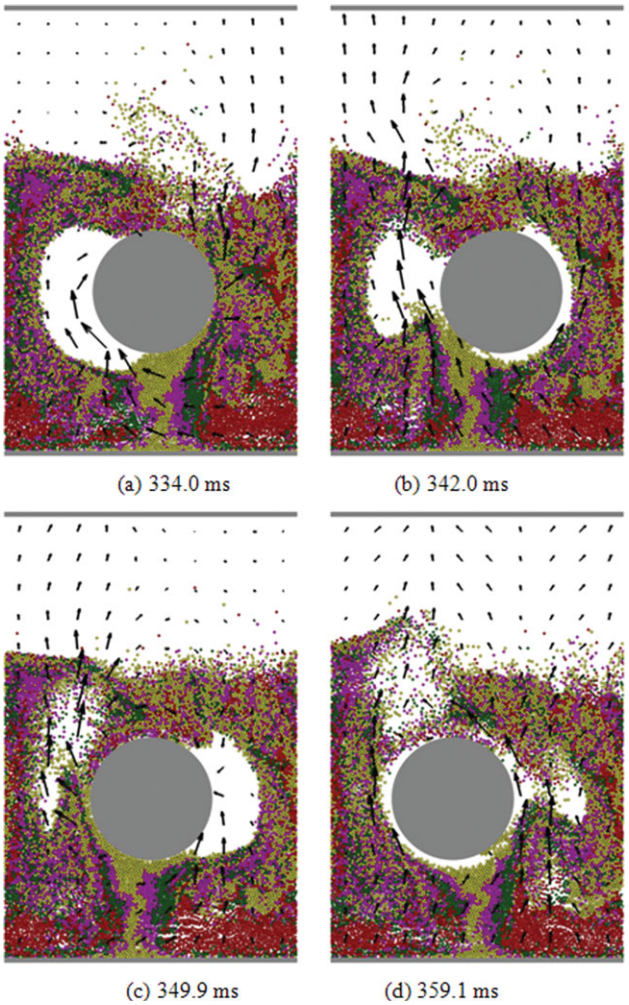


**Figure 6. Gas-fluidized bed with a tube that vibrates horizontally in a sinusoidal motion.**

**Each black arrow represents the local fluid velocity vector averaged over 4 × 4 neighboring fluid cells. The lengths of the arrows, indicating the magnitudes of the fluid velocities, are scaled by the largest one at the current state. [Color figure can be viewed in the online issue, which is available at wileyonlinelibrary.com.]**

boundaries can also be easily modeled when nonstationary tubes are used (i.e., with moving tubes).

*Fluidization with a Stationary Tube.* A two-dimensional (2-D) numerical model of a gas-fluidized bed with a stationary immersed tube is shown in Figure 3. Monosized particles (10,000) ($d_p = 100$ $\mu$m) were generated in a rectangular domain of 12 × 18 mm$^2$ in which a 5 mm diameter disc was located along the central vertical axis and centred at a height of 6.5 mm above the base. The disc represents the cross section of a horizontal cylindrical tube. The material properties of the particles and tube (i.e., disc) are listed in Table 1. Gravity was introduced so that the particles were pluvially deposited to form the initial bed. Then uniform gas was introduced at the bottom of the bed at a constant mass flow rate ($\rho_f \mathbf{u}_f$) and exited from the top boundary across which zero gradients of velocity and pressure were assigned. The initial conditions for the gas are listed in Table 2. The initial superficial gas velocity was 50 mm/s. Periodic boundary conditions were assigned to the lefthand and righthand side boundaries. The powder bed was initially color banded for visualizing the mixing patterns during fluidization.

The simulation results are illustrated in Figure 4. Due to the effect of the presence of the tube on the gas flow, two distinctive features were observed: (1) an air film of variable thickness was intermittently formed below the tube, and (2) a cap of defluidized particles existed above the tube. These results were consistent with the experimental observations.[23] To quantify the observed behavior, an annulus with a thickness of 0.8 mm (i.e., $8d_p$) surrounding the tube is defined (see Figure 3), and this annulus was divided into two halves: top and bottom. The average void fractions in both halves were determined.

Figure 5 shows the time evolution of the average void fractions in the top and bottom halves of this annulus. It is evident that the void fraction in the bottom half is generally higher than that in the top half. This is consistent with the observations shown in Figure 4. It is also found that the void fractions around the tube fluctuate strongly during the process of fluidization. This may be due to the periodic generation and movement of air bubbles. The time instants a–d in Figure 5 correspond to the snapshots (a)–(d) in Figure 4. At instant a, an air film is formed below the tube (Figure 4a), leading to a high-void fraction in the bottom half (Figure 5). As the air film moves upward, it is split around the tube into two bubbles with one on each side of the tube (Figure 4b). The bubbles continue to move up, passing the sides of the tube (Figure 4c). During this period (from a to c), a peak in the void fraction of the top half occurs due to the entrance of the air bubbles into this region. At the same time, some particles flow to the region below the tube causing a decrease of void fraction in the bottom half (Figure 5). As fluidization continues, an air film is created again below the tube (Figure 4d) and the void fraction in the bottom half reaches another peak value (Figure 5). This pattern of events repeats throughout the fluidization process.

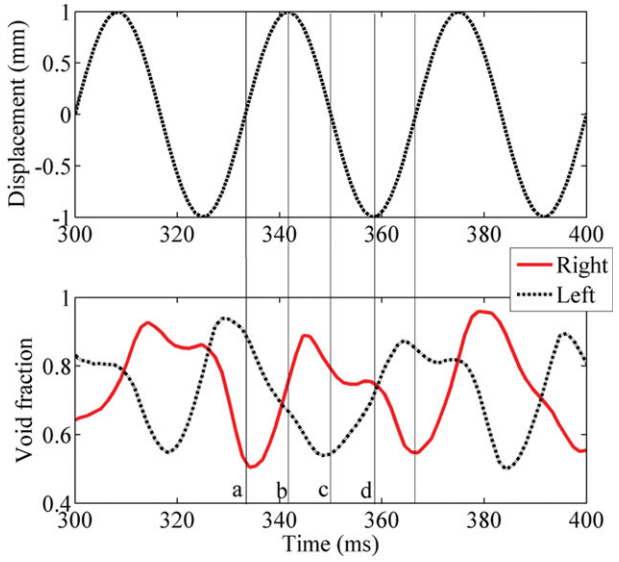


**Figure 7. Tube displacement-time curve (top diagram) and the time evolution of void fractions in the left and right halves of the 0.8 mm thick annulus surrounding the oscillated tube (bottom diagram).**

**[Color figure can be viewed in the online issue, which is available at wileyonlinelibrary.com.]**

**Table 3. Material Properties of the Particles and Box Walls for the Vibrated Bed Simulations**

| | Density ($Kg/m^3$) | Young's modulus (GPa) | Poisson's ratio | Friction coefficient |
|---|---|---|---|---|
| Bronze particles | 8900 | 110 | 0.3 | 0.3 (particle-particle) |
| Glass particles | 2525 | 63 | 0.3 | 0.3 (particle-particle) |
| Box walls | 2525 | 63 | 0.3 | 0.3 (particle-wall) |

*Fluidization with an Oscillating Tube* To promote a uniform heat exchange between the bed and the immersed tube, the solid particles in the neighborhood of the tube should be replaced as frequently as possible. However, the existence of the cap of the defluidized particles above the stationary tube may prevent this as the defluidized particles may be overheated while the other particles have much less chance to contact the tube and be heated. To avoid the defluidized zone, it is proposed to use an oscillating tube that oscillates horizontally in a sinusoidal mode. Besides the curved boundaries which do not conform to the rectangular grid, the IBM can also deal with the moving boundary conditions. Therefore, a fluidized bed with a vibrated tube, the surface of which should be treated as the moving boundary for the gas-particle flow, can be simulated using the proposed method. Figure 6 shows the simulation results of a gas-fluidized bed with a horizontally vibrated tube. The numerical setup of this simulation is the same as that with a stationary tube, as discussed in the previous section, except that a sinusoidal motion is applied to the tube

$$x = A \cdot \sin(2\pi f t) \tag{30}$$

in which, $x$ is the horizontal displacement of the tube relative to the initial position and $t$ is the elapsed time. The amplitude, $A$, and frequency $f$, of the vibrations are set to 1 mm and 30 Hz, respectively. According to the simulation results, no defluidized zone is observed using the vibrated tube and the particles are more uniformly mixed (Figure 6). It is also found that the air film below a horizontally oscillated tube is much thinner than that below a static tube. However, large air bubbles are formed adjacent to the sides of the tube due to the combined effect of fluidization and horizontal movement of the immersed tube.

Figure 7 shows the displacement-time curve for the tube movement and the time evolution of void fractions in the left and right halves of the 0.8 mm thick annulus surrounding the oscillated tube. The displacement is positive (negative) when the tube is located on the right (left) hand side of the initial position. It is observed that the void fractions fluctuate periodically with the same frequency as the vibration of the tube and that the waves in the left side and right side

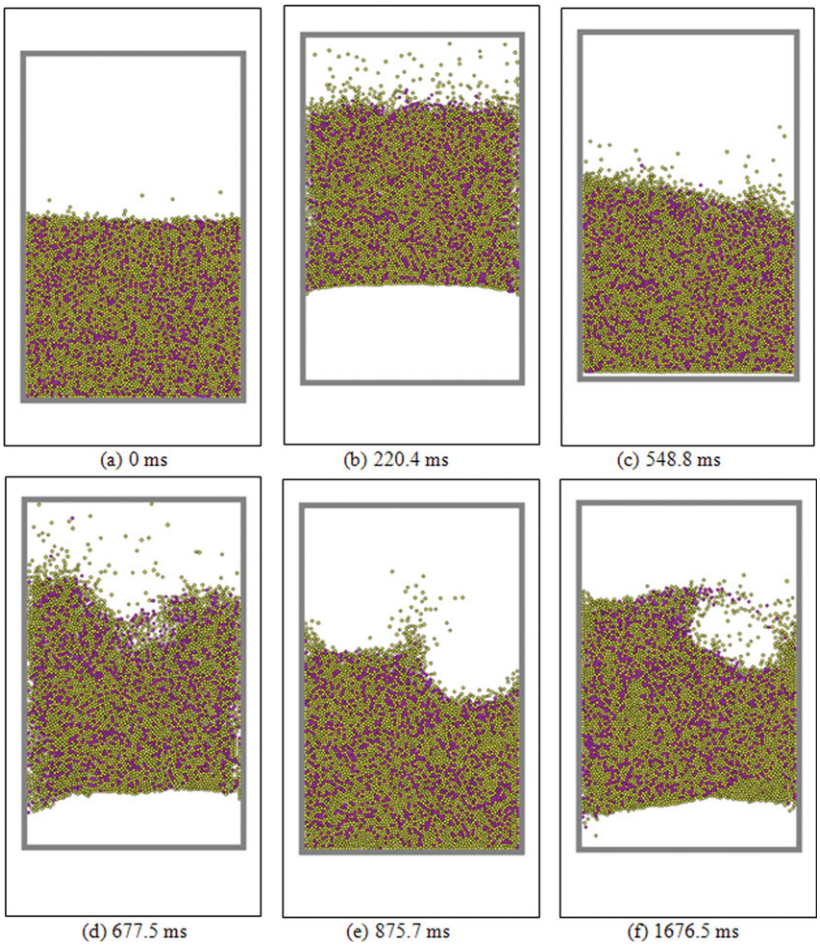


**Figure 8. Behavior of a powder bed vibrated vertically in a sinusoidal motion in a vacuum.**

**The labels represent the elapsed time in millisecond after the start of vibration. The volume ratio of equal-sized bronze particles (colored in magenta) to glass particles (colored in yellow) is 25:75%. The same color coding is also applied in Figures 9 and 11. [Color figure can be viewed in the online issue, which is available at wileyonlinelibrary.com.]**

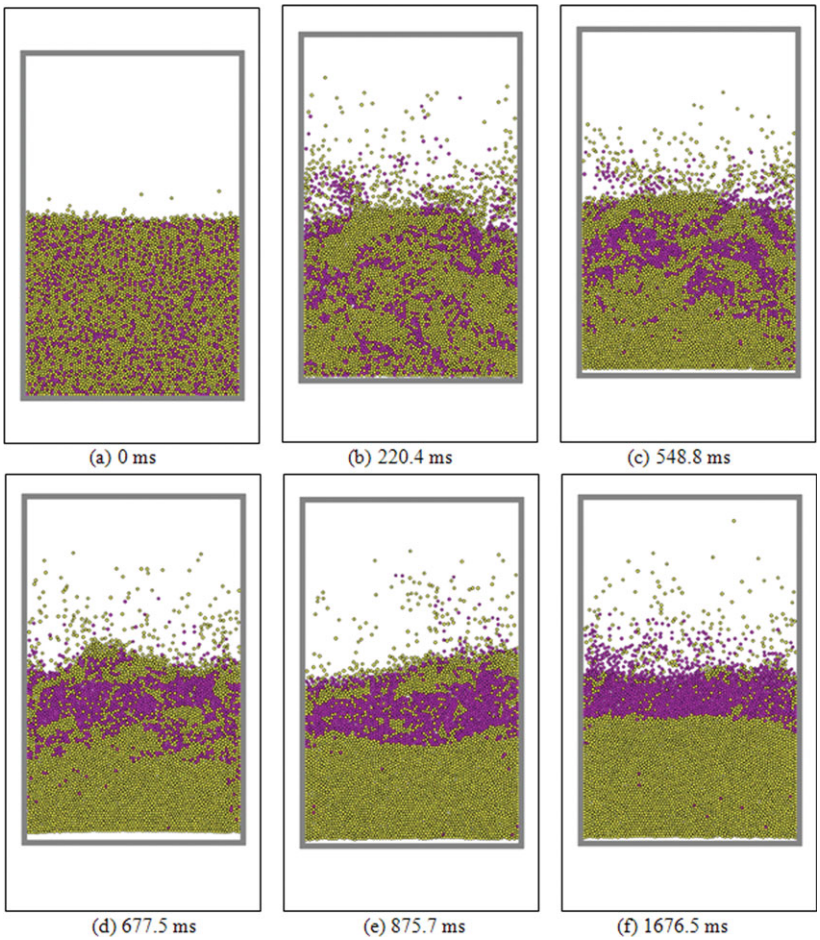


**Figure 9. Air-induced segregation of bronze and glass particles subject to a vertical vibration in the presence of air.**

**[Color figure can be viewed in the online issue, which is available at wileyonlinelibrary.com.]**

are almost in antiphase (i.e., with a phase difference of $\pi$). The time instants a-d in Figure 7 correspond to the snapshots (a)–(d) in Figure 6. When the tube moves back to the original position from the lefthand side at instant a, a large air bubble lags behind the tube (Figure 6a). As the tube moves to the farthest position on the right (Figure 6b) and then goes back to the original position (Figure 6c), an air bubble is gradually generated on the righthand side of the tube. Meanwhile, the air bubble on the lefthand side shrinks and moves upward. During this period (a- c), the void fraction on the right side increases while the void fraction on the left side decreases (Figure 7). As the tube continues to move to the left and then reaches the farthest position on the left (Figure 6d), the bubble on the righthand side shrinks. After the instant d, the tube moves back to the original position, just as the situation at time instant a, and an air bubble is formed on the lefthand side of the tube. From time instant c to the end of the cycle, it is observed that the void fraction on the right side decreases while the void fraction on the left side increases (Figure 7).

In general, a uniform heat exchange between the particles and the tube requires the same chance for all the particles to approach the neighborhood of the tube. In other words, the residence time in the region close to the tube should be similar for each particle. In this work, an index, $I$, is proposed to describe the degree of the dissimilarity of the settling time for the particles

$$I = \sqrt{\frac{1}{N}\sum_{i=1}^{N}\left(\frac{t_i^s - t_{mean}^s}{t_{mean}^s}\right)^2} \tag{31}$$

$$t_{mean}^s = \frac{1}{N}\sum_{i=1}^{N} t_i^s \tag{32}$$

in which, $t_i^s$ represents the cumulative time for the particle $i$ residing in the annulus surrounding the tube during the process (Figure 3), $N$ is the total number of particles in the system (i.e., 10,000 in this simulation), and $t_{mean}^s$ is the mean value of the residence time. From Eq. 31, it can be seen that the index, $I$, is the root mean square of the normalized difference between the residence time of each particle and the mean value. Ideally for a uniform heat exchange, $t_i^s$ is the same for each particle and, therefore, $I$ is equal to zero. The larger the value of $I$, the less uniformly the heat exchange is. According to Eq. 31, for the same duration of fluidization (660 ms), $I$ is calculated as 1.27 for the fluidized bed with a static tube and as 0.82 for the fluidized bed with an oscillating tube. The smaller value of $I$ for the latter case proves that the uniformity of the heat exchange between the particles and tube can be improved by using an oscillated tube.

### *Segregation in vertically vibrated fine granular mixtures*

The segregation of granular mixtures of fine bronze and glass spheres of similar diameters subject to vertical vibrations was first reported by Burtally et al.[29,30] According to

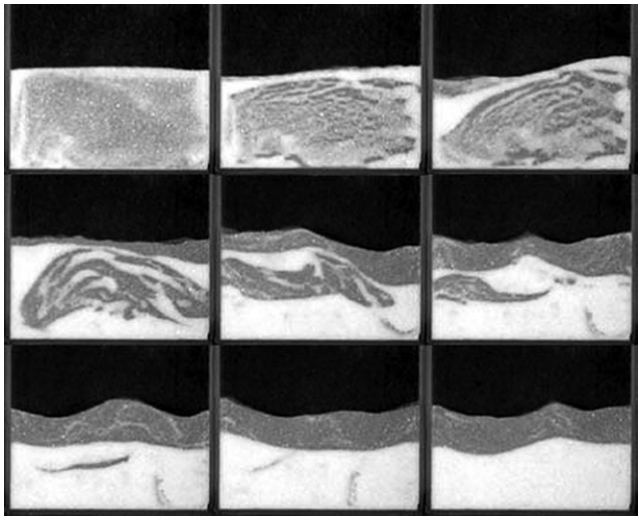

**Figure 10. Experimental observation of air-induced segregation in a vertically vibrated bed by Burtally et al.[30]**

**The volume ratio of the bronze particles (dark) to the glass ones (white) was set to 25:75%. The snapshots form a time sequence from upper left to lower right.**

their experimental observation, the effect of air on the granular motion was believed to be responsible for the segregation and the form (''bronze-on-top'' or ''sandwich'') was dependent on the amplitude and frequency of the vibration. Recently, Zeilstra et al.[31,32] performed numerical studies of this phenomenon using a hybrid granular dynamics-CFD method, and they found the similar results as observed in previous experiments. However, in their simulations, fixed and rectangular computational grids were used and, the lowest computational cells were in general cut by the bottom plate of the vertically vibrated box.[32] Therefore, the bottom boundary for the air flow did not conform to the bottom plate in their simulations. In addition, they used a free-slip boundary condition between the air phase and the box walls. In this study, the IBM was used to model the moving boundaries (walls of the vibrated box) and no-slip boundary conditions were assumed for fluid flow.

Two-dimensional simulations of vertically vibrated beds in a vacuum and in air have been performed. In these simulations, a powder bed consisting of 1250 bronze particles (colored magenta) randomly mixed with 3750 glass particles (colored yellow) is created in a box of dimensions of $8.25 \times 13.2$ mm$^2$. Both particle species have a mean diameter of 110 $\mu$m with a Gaussian size distribution (standard deviation $=$ 10 $\mu$m). This leads to a proportion 25:75% by volume for the bronze particles to the glass ones in the bed. The material properties of the particles and box walls are provided in Table 3.

The box oscillates vertically in a sinusoidal motion defined by

$$y = A \cdot \sin(2\pi f t) \tag{33}$$

where, the amplitude and frequency of vibration are $A = 0.9$ mm and $f = 55$ Hz, respectively. In addition, damping is considered to account for the energy dissipation due to the elastic wave propagation through a solid particle when particle-particle contacts and/or particle-wall contacts occur. The normal damping force $F_{nd}$ and tangential damping force $F_{td}$ are given by

$$F_{nd} = 2\beta\sqrt{m^* K_n}\Delta\delta_n/\Delta t \tag{34}$$

$$F_{td} = 2\beta\sqrt{m^* K_t}\Delta\delta_t/\Delta t \tag{35}$$

in which, $K_n$ and $K_t$ are normal stiffness and tangential stiffness, respectively, and

$$\frac{1}{m^*} = \frac{1}{m_1} + \frac{1}{m_2} \tag{36}$$

$m_1$ and $m_2$ are the masses of two particles in contact and $\beta$ is the damping coefficient. For the particle-wall contact, the mass of the wall is assumed to be much greater than the particle (i.e., $m_2 \gg m_1$) so that $m^*$ is approximately equal to $m_1$. The normal and tangential displacement incremental, $\Delta\delta_n$ and $\Delta\delta_t$, dividing by the time step, $\Delta t$, represent the normal and tangential components of the relative particle velocity at the contact point. The damping forces are added to the normal and

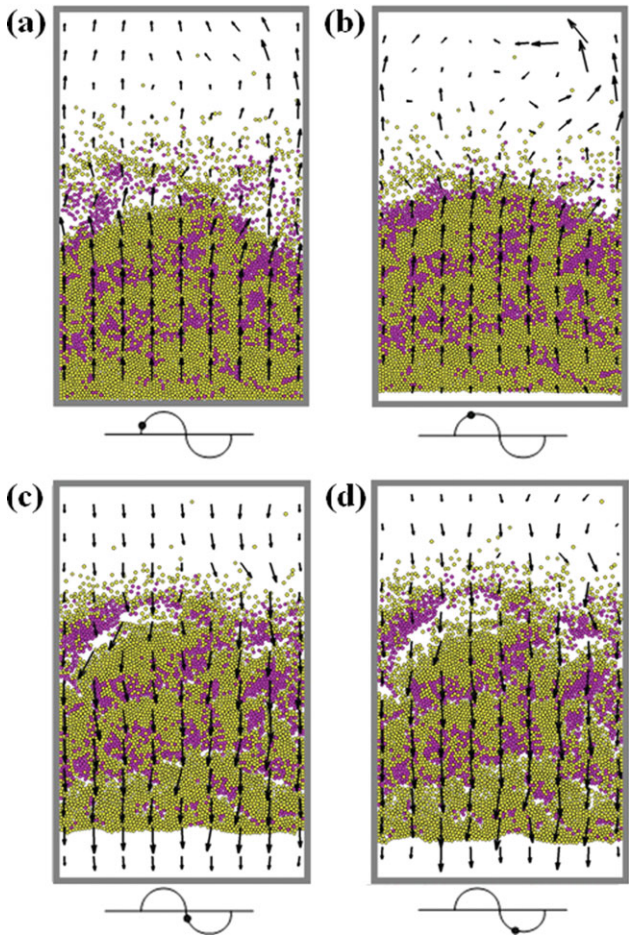


**Figure 11. Compaction and expansion of the powder bed during a single cycle of the vibration in the presence of air.**

**Each black arrow represents the local fluid velocity vector averaged over $3 \times 3$ neighboring fluid cells. The lengths of the arrows, indicating the magnitudes of the fluid velocities, are scaled by the largest one at the current state. [Color figure can be viewed in the online issue, which is available at wileyonlinelibrary.com.]**

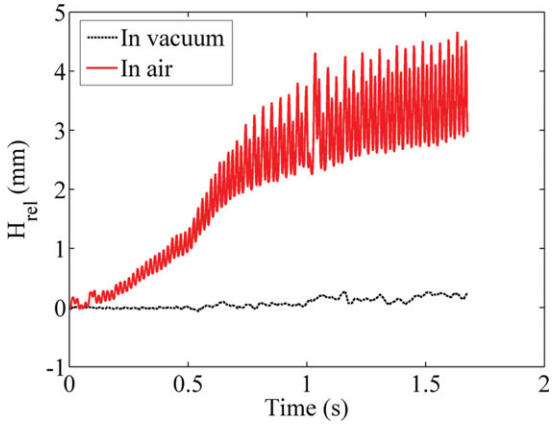


**Figure 12. Time evolution of the average height of the bronze particles relative to the glass ones during vibration in a vacuum and in air.**

**[Color figure can be viewed in the online issue, which is available at wileyonlinelibrary.com.]**

tangential contact forces to provide the contribution to the out-of-balance forces acting on the particles from that contact. In this work, the damping coefficients are assigned as $\beta = 0.048$ for particle-particle damping and $\beta = 0.064$ for particle-wall damping. When air is present, the box is assumed to be a closed system without air leaving or entering. The air inside the box has the initial conditions as shown in Table 2. This set-up is consistent with one of those used in the numerical work of Zeilstra et al.[32]

Figures 8 and 9 show the simulation results in a vacuum and in air, respectively. For vibration in a vacuum, the particles are strongly agitated and the surface of bed becomes severely tilted after the early stage of vibration. No obvious segregation occurs under vacuum conditions (Figure 8). When air is present, clusters of bronze particles are formed gradually and move upward in the bed. Finally, a layer of bronze particles is obtained at the top of the system with a bed of exclusively glass particles at the bottom (Figure 9). The simulation results are in good agreement with previous experimental observations,[30] as shown in Figure 10.

The snapshots at different stages within a cycle of vibration in the presence of air are shown in Figure 11. Red arrows represent the air velocity vectors. As the box moves upward, the powder bed is compacted under the combined effects of gravitational force and the force from the base plate of the box (Figure 11a). When the box almost reaches the highest position, the powder bed continues to move up due to inertia, forming a gap between the bed and the bottom plate (Figure 11b). During this period, the air flows upward. As the box moves downward, the air is forced to flow downward and pass through the powder bed. The bed falls down due to the gravitational force and the air drag. As discussed in our previous work,[21] the particles of lower densities are affected more significantly by the air drag due to the smaller inertia. Therefore, the glass particles, which have a lower density, fall down faster than the bronze particles due to the larger acceleration obtained from the air drag. This causes expansion of the powder bed (Figures.11c and d). In this process, the formation of some voids in the bed provides the space for the downward air flow to entrain the glass particles to the relatively lower region compared to the bronze particles.

The time evolution of the average height of the bronze particles relative to the glass particles during the process of vibration is shown in Figure 12. Under vacuum conditions, the relative height between the bronze and glass particles fluctuates slightly around zero. In the presence of air, the average height of the bronze particles relative to the glass particles increases with significant fluctuations. In general, as the box moves upward the relative height of bronze particles decreases due to the deposition of bronze particles caused by the higher inertia. As the box moves downward the relative height of bronze particles increases because the glass particles are dragged down by the air. The extent of the

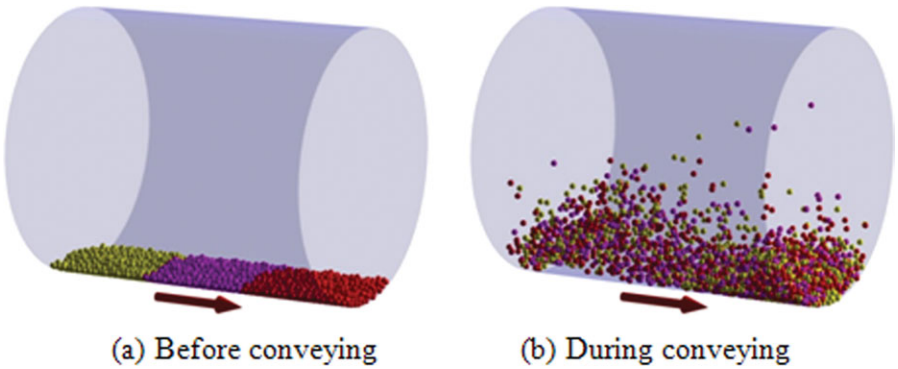


**Figure 13. Snapshots of the initial state (a) and a typical state (b) during pneumatic conveying of granular materials in a cylindrical pipeline.**

**The particles were initially color banded for visualization purposes. Periodic boundary conditions were assigned to two ends of the pipe. The transport of particles was driven by the gas injection at a velocity of 0.5 m/s from the left hand side end. The arrow below the pipe indicates the direction of the flow of gas-particle system. [Color figure can be viewed in the online issue, which is available at wileyonlinelibrary.com.]**

**Table 4. Material Properties of the Particles and Cylindrical Wall for the Pneumatic Conveying Simulations**

| | Density (Kg/m$^3$) | Young's modulus (GPa) | Poisson's ratio | Friction coefficient (Case I) | Friction coefficient (Case II) |
|---|---|---|---|---|---|
| Particles | 2500 | 8.7 | 0.3 | 0.05 (particle-particle) | 0.3 (particle-particle) |
| Cylindrical wall | 7900 | 210 | 0.29 | 0.05 (particle-wall) | 0.3 (particle-wall) |

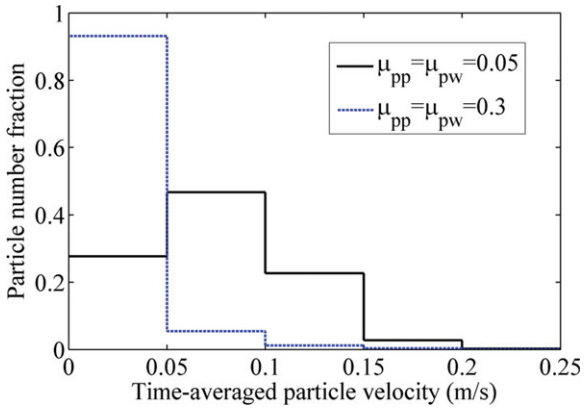


**Figure 14. Particle number fractions as a function of time-averaged particle velocity for different friction coefficients.**

**[Color figure can be viewed in the online issue, which is available at wileyonlinelibrary.com.]**

increase is normally greater than that of the decrease, so that the relative height of bronze particles increases gradually during the vibrating process.

### *Pneumatic conveying in a cylindrical pipeline*

Three-dimensional simulations of pneumatic conveying in a cylindrical pipeline have also been performed, as shown in Figure 13. A monodisperse system with 3,000 particles ($d_p$ = 130 $\mu$m) was generated inside a cylinder with a diameter 6 mm and a length 7.2 mm. The particles are color banded for the visualization of the macroscopic behavior of the particle system. The material properties of the particles and the cylindrical wall are listed in Table 4. Two sets of friction coefficients are used.

For the calculation of gas flow using CFD, the computational domain is meshed by a 3-D rectangular grid. The cylindrical wall is immersed in the grid and the IBM is used to model the gas flow in the boundary cells by treating the cylindrical wall as a no-slip and impermeable boundary. Periodic boundary conditions are applied to the two ends of the pipeline and the gas is injected at a constant mass flow rate at the lefthand side. The gas inside the pipeline has initial conditions as given in Table 2 and the initial gas inflow velocity is 0.5 m/s.

Using the numerical simulations, the effects of particle and wall properties, gas properties, and superficial gas velocity on the transport of particles can be quantitatively explored. Figure 14 shows the particle number fraction as a function of the time-averaged particle velocity for different sets of friction coefficients. With lower friction coefficients ($\mu_{pp} = \mu_{pw} =$ 0.05), the largest number fraction, nearly 50%, is obtained for the particles having a time-averaged velocity in the range 0.05–0.1 m/s. The particle number fractions with velocities in the range 0–0.05 m/s and 0.1–0.15 m/s rank the second and third, respectively. The particles having velocities above 0.15 m/s are only a small fraction. When higher friction coefficients ($\mu_{pp} = \mu_{pw} = 0.3$) are used, the number fraction of particles with velocities above 0.05 m/s is significantly reduced and most of the particles (more than 90%) have velocities below 0.05 m/s. Therefore, as the friction coefficients increase, it becomes more difficult for the particles to be conveyed by the gas and the transport rate of granular materials during pneumatic conveying is consequently reduced.

## Conclusions

An IBM has been developed to model particle laden flows with complex and/or moving boundary conditions. The basic idea of this method is to introduce a virtual body force field such that a desired fluid velocity distribution can be imposed over a solid boundary. The virtual body force acting on a fluid cell is determined by the solid volume fraction and relative velocity of the two phases in a particular cell. By incorporating the IBM into the existing DEM-CFD model, an enhanced method is developed to model the behavior of multiphase systems which involves a fluid, many fine solid particles and one or more LSOs. In this method, the fluid–fine particle interactions are approximated by an empirical correlation for the drag force to achieve low computational cost, while the fluid–large object interaction is solved using the IBM to obtain the detailed information of fluid flow around the object. A significant advantage of the developed method is the ability to handle large objects or arbitrary shaped boundaries whilst still retaining the cost effective discretization of the fluid domain using rectilinear grids.

To illustrate the potential applications of this developed DEM-CFD-IBM approach, case studies have been performed: (1) gas fluidization with an immersed tube, (2) segregation in a vertically vibrated bed, and (3) pneumatic conveying in a cylindrical pipeline. The simulation results have been compared with the previous experimental results available in the literature and it is found that some typical features observed in the physical experiments are also obtained in the present simulations. This broad agreement demonstrates that the developed method is capable of modeling particulate flows consisting of fluids and particles with complex and/or moving boundaries.

## Acknowledgments

This work was financially supported by the Knowledge Transfer Secondments (KTS) grant at the University of Birmingham (Birmingham, UK) during 2010-2011. The authors also acknowledge the University of Birmingham e-Science Cluster for providing computational resources.

## Literature Cited

1. Zhu HP, Zhou ZY, Yang RY, Yu AB. Discrete particle simulation of particulate systems: a review of major applications and findings. *Chem Eng Sci*. 2008;63:5728–5770.
2. Tsuji Y, Tanaka T, Ishida T. Lagrangian numerical simulation of plug flow of cohesionless particles in a horizontal pipe. *Powder Technol*. 1992;71:239–250.
3. Tsuji Y, Kawaguchi T, Tanaka T. Discrete particle simulation of two-dimensional fluidized bed. *Powder Technol*. 1993;77:79–87.
4. Peskin CS. Flow patterns around heart valves: a numerical method. *J Comput Phys*. 1972;10:252–271.
5. Peskin CS. Numerical analysis of blood flow in the heart. *J Comput Phys*. 1977;25:220–252.
6. Mohd-Yusof J. Combined immersed boundaries/B-splines methods for simulations of flows in complex geometries. CTR Annual Research Briefs, NASA Ames/Stanford University; 1997, pp. 317–327.
7. Fadlun EA, Verzicco R, Orlandi P, Mohd-Yusof J. Combined immersed-boundary finite-difference methods for three-dimensional complex flow simulations. *J Comput Phys*. 2000;161:35–60.
8. Mittal R, Iaccarino, G. Immersed boundary methods, *Annu Rev Fluid Mech*. 2005;37:239–261.
9. Liao C-C, Chang Y-W, Lin C-A, McDonough JM. Simulating flows with moving rigid boundary using immersed-boundary method, *Comput Fluids*. 2010;39:152–167.
10. Kajishima T, Takeuchi S, Hamasaki H, Miyake Y. Turbulence structure of particle-laden flow in a vertical plane channel due to vortex shedding. *JSME Int J, Series B*. 2001;44:526–535.
11. Yuki Y, Takeuchi S, Kajishima T. Efficient immersed boundary method for strong interaction problem of arbitrary shape object with the self-induced flow. *J Fluid Sci Tech*. 2007;2:1–11.

12. De Palma P, de Tullio MD, Pascazio G, Napolitano M. An immersed-boundary method for compressible viscous flows. *Comput Fluids*. 2006;35:693–702.
13. de Tullio MD, De Palma P, Iaccarino G, Pascazio G, Napolitano M. An immersed boundary method for compressible flows using local grid refinement. *J Comput Phys*. 2007;225:2098–2117.
14. de' Michieli Vitturi M, Esposti Ongaro T, Neri A, Salvetti MV, Beux F. An immersed boundary method for compressible multiphase flows: application to the dynamics of pyroclastic density currents. *Comput Geosci*. 2007;11:183–198.
15. Kafui KD, Thornton C, Adams MJ. Discrete particle-continuum fluid modelling of gas-solid fluidized beds. *Chem Eng Sci*. 2002;57:2395–2410.
16. Thornton C, Yin KK. Impact of elastic spheres with and without adhesion. *Powder Technol*. 1991;65:153–165.
17. Hertz H. Über die Berührung fester elastischer Körper. *J Reine Angew Math*. 1882;92:156–171.
18. Mindlin RD, Deresiewicz H. Elastic spheres in contact under varying oblique forces. *J Appl Mech*. 1953;20:327–344.
19. Anderson TB, Jackson R. A fluid mechanical description of fluidized beds. Equations of motion. *Ind Eng Chem Fundam*. 1967;6:527–539.
20. Di Felice R. The voidage function for fluid–particle interaction systems. *Int J Multiphase Flow*. 1994;20:153–159.
21. Guo Y, Kafui KD, Wu C-Y, Thornton C, Seville JPK. A coupled DEM/CFD analysis of the effect of air on powder flow during die filling. *AICHE J*. 2009;55:49–62.
22. Wu C-Y, Guo Y. Numerical modelling of suction filling using DEM/CFD. *Chem Eng Sci*. 2012;73:231–238.
23. Glass DH, Harrison D. Flow patterns near a solid obstacle in a fluidized bed. *Chem Eng Sci*. 1964;19:1001–1002.
24. Di Natale F, Bareschino P, Nigro R. Heat transfer and void fraction profiles around a horizontal cylinder immersed in a bubbling fluidised bed. *Int J Heat Mass Transfer*. 2010;53:3525–3532.
25. Rong D, Mikami T, Horio M. Particle and bubble movements around tubes immersed in fluidized beds—a numerical study. *Chem Eng Sci*. 1999;54:5737–5754.
26. Di Maio FP, Di Renzo A, Trevisan D. Comparison of heat transfer models in DEM/CFD simulations of fluidized beds with an immersed probe. *Powder Technol*. 2009;193:257–265.
27. He Y, Zhan W, Zhao Y, Lu H, Schlaberg I. Prediction on immersed tubes erosion using two-fluid model in a bubbling fluidized bed. *Chem Eng Sci*. 2009;64:3072–3082.
28. Yu AB, Xu BH. Particle-scale modelling of gas–solid flow in fluidisation. *J Chem Tech Biotech*. 2003;78:111–121.
29. Burtally N, King PJ, Swift MR. Spontaneous air-driven separation in vertically vibrated fine granular mixtures. *Science* 2002;295:1877–1879.
30. Burtally N, King PJ, Swift MR, Leaper M. Dynamical behaviour of fine granular glass/bronze mixtures under vertical vibration. *Granular Matter*. 2003;5:57–66.
31. Zeilstra C, van der Hoef MA, Kuipers JAM. Simulation study of air-induced segregation of equal-sized bronze and glass particles. *Phys Rev E*. 2006;74:010302(R).
32. Zeilstra C, van der Hoef MA, Kuipers JAM. Simulation of density segregation in vibrated beds. *Phys Rev E*. 2008;77:031309.

## Appendix: Derivation of Pressure-Correction Equations

In this appendix, the pressure-correction equations are derived for 2-D problems, which can be easily extended to 3-D problems. As shown in Figure A1, the fluid quantities are defined at the different locations of the background grid. The fluid velocity vectors (**u**) are located on and perpendicular to the cell faces, and the pressures ($p$) are located in the cell centers. The continuity Eq. 18 for the cell $O$ can be written in a discretization fashion as

$$(\varepsilon_e\rho_f)_O^{n+1} - (\varepsilon_e\rho_f)_O^n + \frac{\Delta t}{\Delta x}[(\varepsilon_e\rho_f u)_2^{n+1} - (\varepsilon_e\rho_f u)_1^{n+1}] + \frac{\Delta t}{\Delta y}[(\varepsilon_e\rho_f u)_4^{n+1} - (\varepsilon_e\rho_f u)_3^{n+1}] = 0 \quad (A1)$$

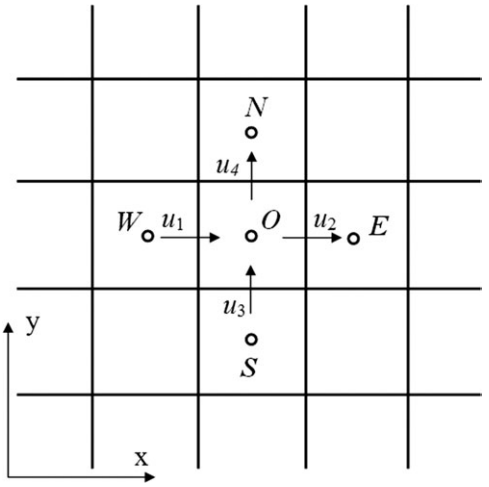


**Figure A1. Staggered locations for the fluid quantities in the field mesh.**

By substituting the virtual body force expression, Eq. 23, the discretized momentum Eq. 21 can be written as

$$(\varepsilon_e\rho_f\mathbf{u})^{n+1} = (1-\alpha)(\varepsilon_e\rho_f\mathbf{u})^n + (1-\alpha)\cdot\Delta t\cdot\mathbf{H}^n - (1-\alpha)\cdot\Delta t\cdot(\varepsilon_e\nabla p)^{n+1} + \alpha\cdot(\varepsilon_e\rho_f\mathbf{U}_{obj})^{n+1} \quad (A2)$$

Substituting the ideal gas law Eq. 12 and replacing the $\rho_f$ at the time step number (n+1) on the righthand side of Eq. A2 gives

$$(\varepsilon_e\rho_f\mathbf{u})^{n+1} = (1-\alpha)(\varepsilon_e\rho_f\mathbf{u})^n + (1-\alpha)\cdot\Delta t\cdot\mathbf{H}^n - (1-\alpha)\cdot\Delta t\cdot(\varepsilon_e\nabla p)^{n+1} + \alpha\frac{M_f}{RT}.(\varepsilon_e p\mathbf{U}_{obj})^{n+1} \quad (A3)$$

By applying (A3) to each face of the cell $O$, we can have

$$(\varepsilon_e\rho_f u)_1^{n+1} = (1-\alpha_1)(\varepsilon_e\rho_f u)_1^n + (1-\alpha_1)\cdot\Delta t\cdot(H_x)_1^n - (1-\alpha_1)\cdot\frac{\Delta t}{\Delta x}\cdot(\varepsilon_e)_1^{n+1}\cdot(p_O^{n+1}-p_W^{n+1}) + \frac{\alpha M_f}{2RT}\cdot(\varepsilon_e)_1^{n+1}\cdot(p_O^{n+1}+p_W^{n+1})\cdot(U_{obj}^x)_1^{n+1} \quad (A4\text{-}1)$$

$$(\varepsilon_e\rho_f u)_2^{n+1} = (1-\alpha_2)(\varepsilon_e\rho_f u)_2^n + (1-\alpha_2)\cdot\Delta t\cdot(H_x)_2^n - (1-\alpha_2)\cdot\frac{\Delta t}{\Delta x}\cdot(\varepsilon_e)_2^{n+1}\cdot(p_E^{n+1}-p_O^{n+1}) + \frac{\alpha M_f}{2RT}\cdot(\varepsilon_e)_2^{n+1}\cdot(p_O^{n+1}+p_E^{n+1})\cdot(U_{obj}^x)_2^{n+1} \quad (A4\text{-}2)$$

$$(\varepsilon_e\rho_f u)_3^{n+1} = (1-\alpha_3)(\varepsilon_e\rho_f u)_3^n + (1-\alpha_3)\cdot\Delta t\cdot(H_y)_3^n - (1-\alpha_3)\cdot\frac{\Delta t}{\Delta y}\cdot(\varepsilon_e)_3^{n+1}\cdot(p_O^{n+1}-p_S^{n+1}) + \frac{\alpha M_f}{2RT}\cdot(\varepsilon_e)_3^{n+1}\cdot(p_O^{n+1}+p_S^{n+1})\cdot(U_{obj}^y)_3^{n+1} \quad (A4\text{-}3)$$

$$(\varepsilon_e\rho_f u)_4^{n+1} = (1-\alpha_4)(\varepsilon_e\rho_f u)_4^n + (1-\alpha_4)\cdot\Delta t\cdot(H_y)_4^n - (1-\alpha_4)\cdot\frac{\Delta t}{\Delta y}\cdot(\varepsilon_e)_4^{n+1}\cdot(p_N^{n+1}-p_O^{n+1}) + \frac{\alpha M_f}{2RT}\cdot(\varepsilon_e)_4^{n+1}\cdot(p_O^{n+1}+p_N^{n+1})\cdot(U_{obj}^y)_4^{n+1} \quad (A4\text{-}4)$$

in which, $H_x$ and $H_y$ are the x- and y-components, respectively, of the vector **H** defined by Eq. 22. In addition, $U^x_{obj}$ and $U^y_{obj}$ are the x- and y-components, respectively, of the local LSO velocity vector $\mathbf{U}_{obj}$.

The actual pressure field at the time step number (n+1), $p^{n+1}$, can be written as a sum of the predicted field, $p^*$, and the corrected field $p'$, that is

$$p^{n+1} = p^* + p' \tag{A5}$$

The predicted pressure field, $p^*$, leads to the predicted mass flow field, $\varepsilon_e\rho_f\mathbf{u}$, as follows

$$(\varepsilon_e\rho_f u)_1^* = (1-\alpha_1)(\varepsilon_e\rho_f u)_1^n + (1-\alpha_1)\cdot\Delta t\cdot(H_x)_1^n - (1-\alpha_1)\cdot\frac{\Delta t}{\Delta x}\cdot(\varepsilon_e)_1^{n+1}\cdot(p_O^* - p_W^*) + \frac{\alpha M_f}{2RT}\cdot(\varepsilon_e)_1^{n+1}\cdot(p_O^* + p_W^*)\cdot(U^x_{obj})_1^{n+1} \tag{A6-1}$$

$$(\varepsilon_e\rho_f u)_2^* = (1-\alpha_2)(\varepsilon_e\rho_f u)_2^n + (1-\alpha_2)\cdot\Delta t\cdot(H_x)_2^n - (1-\alpha_2)\cdot\frac{\Delta t}{\Delta x}\cdot(\varepsilon_e)_2^{n+1}\cdot(p_E^* - p_O^*) + \frac{\alpha M_f}{2RT}\cdot(\varepsilon_e)_2^{n+1}\cdot(p_O^* + p_E^*)\cdot(U^x_{obj})_2^{n+1} \tag{A6-2}$$

$$(\varepsilon_e\rho_f u)_3^* = (1-\alpha_3)(\varepsilon_e\rho_f u)_3^n + (1-\alpha_3)\cdot\Delta t\cdot(H_y)_3^n - (1-\alpha_3)\cdot\frac{\Delta t}{\Delta y}\cdot(\varepsilon_e)_3^{n+1}\cdot(p_O^* - p_S^*) + \frac{\alpha M_f}{2RT}\cdot(\varepsilon_e)_3^{n+1}\cdot(p_O^* + p_S^*)\cdot(U^y_{obj})_3^{n+1} \tag{A6-3}$$

$$(\varepsilon_e\rho_f u)_4^* = (1-\alpha_4)(\varepsilon_e\rho_f u)_4^n + (1-\alpha_4)\cdot\Delta t\cdot(H_y)_4^n - (1-\alpha_4)\cdot\frac{\Delta t}{\Delta y}\cdot(\varepsilon_e)_4^{n+1}\cdot(p_N^* - p_O^*) + \frac{\alpha M_f}{2RT}\cdot(\varepsilon_e)_4^{n+1}\cdot(p_O^* + p_N^*)\cdot(U^y_{obj})_4^{n+1} \tag{A6-4}$$

Using the correlation Eq. A5, the subtraction of Eq. A6 from Eq. A4 gives

$$(\varepsilon_e\rho_f u)_1^{n+1} = (\varepsilon_e\rho_f u)_1^* - (1-\alpha_1)\cdot\frac{\Delta t}{\Delta x}\cdot(\varepsilon_e)_1^{n+1}\cdot(p'_O - p'_W) + \frac{\alpha M_f}{2RT}\cdot(\varepsilon_e)_1^{n+1}\cdot(p'_O + p'_W)\cdot(U^x_{obj})_1^{n+1} \tag{A7-1}$$

$$(\varepsilon_e\rho_f u)_2^{n+1} = (\varepsilon_e\rho_f u)_2^* - (1-\alpha_2)\cdot\frac{\Delta t}{\Delta x}\cdot(\varepsilon_e)_2^{n+1}\cdot(p'_E - p'_O) + \frac{\alpha M_f}{2RT}\cdot(\varepsilon_e)_2^{n+1}\cdot(p'_O + p'_E)\cdot(U^x_{obj})_2^{n+1} \tag{A7-2}$$

$$(\varepsilon_e\rho_f u)_3^{n+1} = (\varepsilon_e\rho_f u)_3^* - (1-\alpha_3)\cdot\frac{\Delta t}{\Delta y}\cdot(\varepsilon_e)_3^{n+1}\cdot(p'_O - p'_S) + \frac{\alpha M_f}{2RT}\cdot(\varepsilon_e)_3^{n+1}\cdot(p'_O + p'_S)\cdot(U^y_{obj})_3^{n+1} \tag{A7-3}$$

$$(\varepsilon_e\rho_f u)_4^{n+1} = (\varepsilon_e\rho_f u)_4^* - (1-\alpha_4)\cdot\frac{\Delta t}{\Delta y}\cdot(\varepsilon_e)_4^{n+1}\cdot(p'_N - p'_O) + \frac{\alpha M_f}{2RT}\cdot(\varepsilon_e)_4^{n+1}\cdot(p'_O + p'_N)\cdot(U^y_{obj})_4^{n+1} \tag{A7-4}$$

According to the ideal gas law, Eq. 12, the first two terms in Eq. A1 can be written as

$$(\varepsilon_e\rho_f)_O^{n+1} = (\varepsilon_e)_O^{n+1}\cdot\frac{M_f}{RT}\cdot p_O^{n+1} = (\varepsilon_e)_O^{n+1}\cdot\frac{M_f}{RT}\cdot(p_O^* + p'_O) \tag{A8}$$

$$(\varepsilon_e\rho_f)_O^{n} = (\varepsilon_e)_O^{n}\cdot\frac{M_f}{RT}\cdot p_O^{n} \tag{A9}$$

By substituting Eqs. A7, A8, and A9 into Eq. A1 and reorganizing the equation, the pressure-correction equation for the cell $O$ can be obtained as

$$a_O p'_O + (a'_W + a''_W)p'_W + (a'_E + a''_E)p'_E + (a'_S + a''_S)p'_S + (a'_N + a''_N)p'_N = b \tag{A10}$$

in which,

$$a^I_W = (1-\alpha_1)(\varepsilon_e)_1^{n+1}\left(\frac{\Delta t}{\Delta x}\right)^2 \tag{A11}$$

$$a^{II}_W = \frac{\Delta t}{\Delta x}\cdot\frac{\alpha M_f}{2RT}(\varepsilon_e)_1^{n+1}(U^x_{obj})_1^{n+1} \tag{A12}$$

$$a^I_E = (1-\alpha_2)(\varepsilon_e)_2^{n+1}\left(\frac{\Delta t}{\Delta x}\right)^2 \tag{A13}$$

$$a^{II}_E = -\frac{\Delta t}{\Delta x}\cdot\frac{\alpha M_f}{2RT}(\varepsilon_e)_2^{n+1}(U^x_{obj})_2^{n+1} \tag{A14}$$

$$a^I_S = (1-\alpha_3)(\varepsilon_e)_3^{n+1}\left(\frac{\Delta t}{\Delta y}\right)^2 \tag{A15}$$

$$a^{II}_S = \frac{\Delta t}{\Delta y}\cdot\frac{\alpha M_f}{2RT}(\varepsilon_e)_3^{n+1}(U^y_{obj})_3^{n+1} \tag{A16}$$

$$a^I_N = (1-\alpha_4)(\varepsilon_e)_4^{n+1}\left(\frac{\Delta t}{\Delta y}\right)^2 \tag{A17}$$

$$a^{II}_N = -\frac{\Delta t}{\Delta y}\cdot\frac{\alpha M_f}{2RT}(\varepsilon_e)_4^{n+1}(U^y_{obj})_4^{n+1} \tag{A18}$$

$$a_O = a^{II}_W - a^I_W + a^{II}_E - a^I_E + a^{II}_S - a^I_S + a^{II}_N - a^I_N - (\varepsilon_e)_O^{n+1}\cdot\frac{M_f}{RT} \tag{A19}$$

and

$$b = (\varepsilon_e)_O^{n+1}\cdot\frac{M_f}{RT}\cdot p_O^* - (\varepsilon_e)_O^n\cdot\frac{M_f}{RT}\cdot p_O^n + \frac{\Delta t}{\Delta x}[(\varepsilon_e\rho_f u)_2^* - (\varepsilon_e\rho_f u)_1^*] + \frac{\Delta t}{\Delta y}[(\varepsilon_e\rho_f u)_4^* - (\varepsilon_e\rho_f u)_3^*] = (\varepsilon_e)_O^{n+1}\cdot\rho_O^* - (\varepsilon_e)_O^n\cdot\rho_O^n + \frac{\Delta t}{\Delta x}[(\varepsilon_e\rho_f u)_2^* - (\varepsilon_e\rho_f u)_1^*] + \frac{\Delta t}{\Delta y}[(\varepsilon_e\rho_f u)_4^* - (\varepsilon_e\rho_f u)_3^*] \tag{A20}$$

Similarly, the pressure-correction equations can be obtained for all the fluid cells, and the corrected pressure in each cell can be determined by solving this set of linear equations.

*Manuscript received Apr. 12, 2012, and revision received July 5, 2012.*